Research Square

Preprints are preliminary reports that have not undergone peer review.
They should not be considered conclusive, used to inform clinical practice,
or referenced by the media as validated information.

High-performance electroluminescent LEDs via structural engineering of ultrasound-assisted carbon quantum dots

Jinxing Zhao

jxzhao@hbu.edu.cn

Hebei University https://orcid.org/0000-0003-4448-2219

Ziyi Liu

Hebei University

Xu Li

Hebei University

Jiayun Li

Hebei University

Binghan Liu

Hebei University

Longxue Zheng

Hebei University

Li Guan

Hebei University

Zhan'ao Tan

Beijing University of Chemical Technology https://orcid.org/0000-0003-2700-4725

Article

Keywords:

Posted Date: September 9th, 2026

DOI: https://doi.org/10.21203/rs.3.rs-10944446/v1

License: This work is licensed under a Creative Commons Attribution 4.0 International License.
Read Full License

Additional Declarations: There is **NO** Competing Interest.

High-performance electroluminescent LEDs via structural engineering of ultrasound-assisted carbon quantum dots

Ziyi Liu[1], Xu Li[1*], Jiayun Li[1], Binghan Liu[1], Longxue Zheng[1], Li Guan[1*], Zhan'ao Tan[2*], Jinxing Zhao[1*]

[1]Hebei Key Laboratory of Optic-electronic Information and Materials, College of Physics Science and Technology, Hebei University, Baoding, China.
[2]State Key Laboratory of Chemical Resource Engineering, Beijing Advanced Innovation Center for Soft Matter Science and Engineering, Beijing University of Chemical Technology, Beijing, China.

E-mail: lixcn@sina.com; lguan@hbu.edu.cn; tanzhanao@mail.buct.edu.cn; jxzhao@hbu.edu.cn

ABSTRACT: Carbon quantum dots (CQDs) have emerged as eco-friendly luminescent nanomaterials, offering a low-toxicity alternative to heavy metal-based quantum dots for optoelectronic applications. However, the harsh synthesis conditions of CQDs and the difficulty in tuning their optical properties hinder their application in CQD light-emitting diodes (CQD-LEDs). Here, we report a rapid gram-scale synthesis of matrix-free solid-state fluorescent CQDs via an ultrasonic-assisted method (UA-CQDs). Experimental and theoretical analyses reveal that structural engineering via tailored biphenyl structures enhances steric hindrance, suppresses π–π stacking, and significantly boosts solid-state fluorescence intensity with a nearly fixed emission wavelength, achieving a 63% increase. By leveraging these UA-CQDs, high-performance CQD-LEDs are fabricated. Devices using UA-CQDs directly as the emissive layer achieve a record luminance of 7774 cd m^{-2} among undoped green CQD-LEDs. Furthermore, a record-high maximum EQE of 12.2% is achieved by employing a thermally activated sensitized fluorescence (TSF) mechanism. Through device structure optimization, a peak luminance of 19,043 cd m^{-2} is subsequently realized, both representing the highest among reported CQD-LEDs. This work provides a simple and generalizable strategy for advancing CQD-LEDs technology.

Introduction

Light-emitting diodes (LEDs) have emerged as a key next-generation technology in display and lighting applications, leveraging core advantages such as ultra-high energy efficiency, wide color gamut, extended lifespan, and miniaturization [1-3]. With the growing demand for high-performance display technologies, perovskite-based LEDs (PeLEDs) [4] and quantum dot LEDs (QLEDs) [5,6] have garnered significant attention due to their outstanding performance characteristics, positioning them as promising candidates for next-generation displays. However, most high-performance devices rely on heavy metals such as cadmium (Cd) and lead (Pb), whose high toxicity has raised concerns about health and environmental safety. Given these considerations, many researchers have focused on developing low-toxicity or metal-free luminescent materials and have made significant progress.

As a new low-toxicity member of the carbon nanomaterial family, carbon dots have garnered significant attention since their discovery in 2004 [7], owing to their excellent optical properties and wide availability of precursor choices. Researchers widely use the hydrothermal method to synthesize carbon quantum dots (CQDs) because of its compatibility with various precursors [8]. Hydrothermal/solvothermal methods [9] yield numerous high-performance CQDs, which have been applied in fields including tumor therapy [10-12], laser technology [13,14], and anti-counterfeiting [15], with notable progress particularly in CQD-based light-emitting diodes (CQD-LEDs) [16,17].

However, the hydrothermal method requires relatively high reaction temperatures, pressures, and durations, making large-scale synthesis challenging. Moreover, this "black-box" synthesis approach obscures the relationship between precursor structure and CQDs' performance. Reliance on extensive experimental screening of precursors and reaction conditions to obtain high-quality CQDs limits research progress. Therefore, simplifying CQD synthesis while achieving theoretically designed, controllable performance remains a major challenge. To address these challenges, the ultrasonic-assisted approach offers advantages in terms of speed, yield, energy consumption, and safety compared with the hydrothermal method. Ultrasound generates cavitation effects in liquids, in which mechanical energy transfer accelerates chemical reactions [18]. Within the field of nanomaterials, researchers have widely applied ultrasound technology [19-25].

In this work, we report the ultrasonic-assisted synthesis of matrix-free solid-state fluorescent CQDs. A Knoevenagel condensation-based cascade reaction driven by ultrasonic cavitation produces highly luminescent CQDs, termed ultrasonic-assisted CQDs (UA-CQDs), on a gram scale within 0.5 h at ambient temperature. Through precursor design, CQDs with tailored compositions and structures are constructed to enhance performance. Density functional theory (DFT) calculations indicate that introducing steric structures confers resistance to fluorescence quenching caused by π–π stacking interactions. Notably, replacing the naphthalene moiety with a spatially extended non-planar biphenyl structure further enhances this resistance. Consequently, the solid-state photoluminescence quantum yield (PLQY) of the corresponding CQDs is increased from 14% to 23%, significantly optimizing their optical performance. Given the excellent optical properties and good film-forming capability of UA-CQDs, high-performance UA-CQD-based light-emitting diodes (UA-CQD-LEDs) were fabricated. By constructing the emitting layer using a host-guest system with a thermally activated delayed fluorescence (TADF) material as the host, a record-high maximum EQE of 12.2% was achieved. Furthermore, through device structure optimization, a peak luminance of 19,043 cd m^{-2} was realized. To the best of our knowledge, the EQE and peak luminance of our devices each represent the highest values in the CQD-LED field. These results demonstrate the successful fabrication of high-performance, heavy-metal-free CQD-LEDs, and offer a viable pathway toward sustainable LED technologies.

Results and Discussion

Synthesis of UA-CQDs

For the ultrasonic-assisted synthesis of solid-state fluorescent CQDs, the aldehyde-containing precursor 4,4'-diformalyltriphenylamine was allowed to react with active methylene precursors in ethanol. Subsequently, sodium hydroxide was added to establish a strongly basic solution environment. Under ambient temperature and pressure conditions, ultrasonic treatment was performed for 0.5 h using a ultrasonic cleaner, and UA-CQDs were obtained. **Fig. 1a and Supplementary Fig. 1** illustrate the reaction mechanism, process, and applications of UA-CQDs.

Under ambient temperature and pressure, we constructed an experimental setup **(Fig. 1b)** to perform *in situ* spectroscopic measurements on CQDs, further analyzing the synthesis process of UA-CQDs. *In situ* photoluminescence (PL) spectra **(Figs. 1c and 1d)** reveal that a distinct fluorescence peak appears within 5 min, which indicates that the Knoevenagel condensation had initiated. As more product accumulated, it exceeded its solubility in ethanol and precipitated. The emission peak gradually red-shifted to 570 nm as the reaction progressed, along with a significant increase in intensity. After 0.5 h of reaction, the massive formation and aggregation of UA-CQDs resulted in bright yellow fluorescence, and led to a stabilized emission spectrum with a peak position identical to that in their solid state. Beyond the rapid and simple synthesis, the one-pot gram-scale synthesis of UA-CQDs was achieved by scaling up the reaction **(Fig. 1e)**, yielding 1.376 g. UA-CQDs can be produced on a significantly larger scale compared to conventional quantum dot materials. The stability of UA-CQDs was assessed by dispersing them in solutions at various pH levels for one year **(Supplementary Fig. 2)**. Their PL spectra were then measured in dichloromethane at the same concentration **(Fig. 1f)**, and the results show that compared with the freshly prepared sample, UA-CQDs stored for one year retain more than 94% of their original fluorescence intensity, demonstrating excellent acid-base stability and water resistance. By substituting different precursors containing aldehyde groups and active methylene groups, the preparation of solid-state fluorescent CQDs emitting from green to near-infrared regions can be prepared via an ultrasonic-assisted synthesis method **(Supplementary Figs. 3, 4 and Supplementary Table 1)**, demonstrating the broad applications of this strategy. Unexpectedly, we found that replacing 2-naphthylacetonitrile with 4-biphenylacetonitrile as the precursor did not significantly shift the emission wavelength of the resulting UA-CQDs (within 10 nm), but markedly enhanced their solid-state fluorescence intensity. In the field of quantum dots, optimization methods for enhancing fluorescence intensity have primarily focused on constructing core-shell structures or optimizing surface ligands. The impact of precursor structure on the luminescent properties of most CQDs remains unclear and difficult to predict. The phenomenon of fluorescence intensity changes caused by intrinsic structural variations is relatively rare, which has drawn our attention. We named these two types of CQDs N-UA-CQDs and B-UA-CQDs for further analysis.

Both B-UA-CQDs and N-UA-CQDs are soluble in various common organic solvents. When dissolved in 1,4-dioxane, both UA-CQDs exhibit a vivid yellow color under daylight and bright green fluorescence under 365 nm UV light. **Fig. 1g** shows the UV-vis absorption spectrum and PL spectrum of B-UA-CQDs, and the B-UA-CQDs solution exhibits well-defined absorption peaks at 256 nm, 297 nm, and 434 nm, while displaying a single emission peak at 508 nm with a full width at half maximum (FWHM) of 63 nm. N-UA-CQDs exhibit similar optical characteristics, with an emission peak at 503 nm and an FWHM of 68 nm **(Supplementary Fig. 5)**.

Structure of UA-CQDs

Structural characterizations were performed to analyze the structure and differences between the two types of UA-CQDs. Transmission electron microscopy (TEM) images **(Fig. 2a and Supplementary Fig. 6)**

reveal that both types of UA-CQDs exhibit uniformly dispersed spherical particles. The average particle sizes of B-UA-CQDs and N-UA-CQDs were determined to be 4.28 nm and 4.22 nm, respectively. Corresponding high-resolution TEM (HRTEM) images show that both types of UA-CQDs possess lattice fringes with a spacing of 0.21 nm, which corresponds to the (100) facets of graphitic carbon [26]. Atomic force microscopy (AFM) shows that both types of UA-CQDs have a height of approximately 4 nm **(Supplementary Fig. 7)**, which is consistent with the HRTEM results, indicating that these two types of UA-CQDs are spherical or ellipsoidal CQDs. This provides direct evidence for the successful synthesis of these two UA-CQDs.

Further structural analysis via X-ray diffraction (XRD) **(Fig. 2b)** reveals that both UA-CQDs exhibit a weak broad peak at 22.5°, corresponding to a d-spacing of 0.39 nm. Due to the small size of the CQDs, the combined effects of steric hindrance from surface functional groups and interlayer distortion caused by specific units within the carbon core lead to an expanded interlayer spacing [27]. In addition, distinct diffraction peaks can be observed for both UA-CQDs, with those of B-UA-CQDs being more prominent. This phenomenon is attributed to the mutual overlap of the edge functional groups of CQDs and their constituent partially crystalline regions [28,29], indicating that B-UA-CQDs are characterized by relatively more crystalline regions and higher packing density in the solid state. In a simple dialysis experiment **(Supplementary Fig. 8)**, for each type of UA-CQDs, dialysis was performed using membranes with molecular weight cut-offs (MWCO) of 5000 Da and 20,000 Da. No CQDs escaped from the 5000 Da MWCO membrane, while only a small amount leaked out from the 20,000 Da MWCO bag, showing weak green fluorescence. This result demonstrates their high molecular weight and relatively large particle size that are consistent with the typical characteristics of CQDs. Through Gel Permeation Chromatography (GPC) **(Fig. 2c)**, we further determined the molecular weights (Mw) of B-UA-CQDs and N-UA-CQDs: 26,389 and 26,061, respectively. These values align with the typical molecular weights of CQDs [30]. Together with the TEM images and XRD patterns, these results suggest that UA-CQDs are spherical particles containing partially graphitized structures, surrounded by a disordered arrangement of surface functional groups.

Moreover, the specific chemical bonds and functional groups of UA-CQDs were further analyzed by Fourier transform infrared (FT-IR) spectroscopy. As shown in **Figs. 2d and 2e**, the broad bands in the range of 3094–2837 cm^{-1} are attributed to aliphatic C-H stretching vibrations. For B-UA-CQDs, a distinct peak at 2207 cm^{-1} is attributed to the C≡N group originating from the precursor 4-biphenylacetonitrile; a similar peak is observed for N-UA-CQDs derived from 2-naphthylacetonitrile. The peaks at 1510 cm^{-1} and 1408 cm^{-1} are assigned to the C=C stretching vibrations of the aromatic rings. The relatively stronger peaks at 1323 cm^{-1} and 1276 cm^{-1} are attributed to the C-N stretching vibrations [31]. In addition, the characteristic peaks appearing in the range of 838–695 cm^{-1} are attributed to out-of-plane bending vibrations of C-H bonds on the aromatic rings. Within this region, a small peak at 668 cm^{-1} is observed for B-UA-CQDs, while a more pronounced sharp peak at 815 cm^{-1} is observed for N-UA-CQDs. This difference arises from the fused-ring nature of naphthalene and the mono-substituted benzene ring of biphenyl.

The elemental composition and chemical bonds of the two UA-CQDs were analyzed using X-ray photoelectron spectroscopy (XPS) **(Figs. 2f and 2h)**. The full XPS spectra **(Supplementary Figs. 9 and 10)** reveal that both UA-CQDs primarily consist of C and N elements, with trace oxygen. Characteristic peaks are observed in the high-resolution C 1s spectrum of B-UA-CQDs at C=C/C-C (284.8 eV), C-N/C≡N (285.3 eV), confirming that the CQDs feature an aromatic carbon skeleton. The preservation of the precursor structure is further demonstrated by fitting the high-resolution N 1s spectrum, with C≡N

(399.5 eV) corresponding to the cyano group and C-N (400.4 eV) corresponding to the triphenylamine unit. Similar results are observed for N-UA-CQDs.

Nuclear magnetic resonance (NMR) spectroscopy was employed to analyze the chemical composition of UA-CQDs and their synthesis process **(Fig. 2g, Supplementary Figs. 11 and 12)**. By comparing the ^{13}C and ^{1}H NMR signals of B-UA-CQDs with those of the two respective precursors, the highly reactive aldehyde group in precursor 4,4'-diformyltriphenylamine (^{13}C: 191.2 ppm, ^{1}H: 9.8 ppm) and the corresponding reactive site in precursor 4-biphenylacetonitrile, the active methylene group (^{13}C: 22.0 ppm, ^{1}H: 4.1 ppm), are almost completely absent in B-UA-CQDs. This confirms that the cascade reaction based on the Knoevenagel reaction has proceeded to completion. The three aromatic carbons connected to the central nitrogen in 4,4'-diformyltriphenylamine (^{13}C: 151.4 ppm, 145.0 ppm) are observed in the ^{13}C NMR signals of B-UA-CQDs (^{13}C: 143.5–141.0 ppm). Due to increased electron density and enhanced shielding, these signal shifts toward higher field strengths. The cyano group in 4-biphenylacetonitrile (^{13}C: 119.2 ppm) is similarly retained in B-UA-CQDs (^{13}C: 118.6 ppm). The formation of the -CH=C-C≡N structure are observed in the ^{13}C NMR signals of B-UA-CQDs at 148.9 ppm and 118.6 ppm. A consistent pattern of disappearance and retention of specific functional groups and sites during the reaction is observed in those of N-UA-CQDs, indicating that both UA-CQDs follow the same reaction pathway. Additionally, B-UA-CQDs exhibit characteristic peaks at 140.1 ppm and 141.7 ppm that are absent in those of N-UA-CQDs, indicating the retention of the biphenyl structure from the precursor.

Based on the high-resolution mass (HR-MS) results, the primary fragments of UA-CQDs consist of one aldehyde-containing triphenylamine derivative and two active methylene-containing precursors formed via condensation and dehydration, with *m/z* ratios of 599 and 651, respectively **(Supplementary Fig. 13)**. Combined these results with the above structural characterization, the synthetic process of N-UA-CQDs and B-UA-CQDs is reasonably inferred to proceed as follows **(Supplementary Fig. 14)**: initial units are rapidly formed via condensation between one triphenylamine derivative and two active methylene precursors under NaOH catalysis, followed by internal carbonization among these units driven by ultrasonic energy, forming partially graphitized structures. With prolonged reaction time, the intermediate products are further grown, carbonized, and finally surface-functionalized, ultimately yielding UA-CQDs.

Theoretical Calculation Analysis

To analyze the solid-state fluorescence generation mechanism of UA-CQDs and the cause of the unique fluorescence intensity enhancement observed upon replacing 2-naphthylacetonitrile with 4-biphenylacetonitrile, DFT calculations were performed. Three CQD models were constructed: pure aromatic skeleton CQDs (A-CQDs); A-CQDs passivated with one triphenylamine unit and one (naphthalene)-C(CN)=CH- unit (NTA-CQDs); and A-CQDs passivated with one triphenylamine unit and one (biphenyl)-C(CN)=CH- unit (BTA-CQDs). Based on Zhao et al.'s theoretical calculations on triphenylamine-derived carbon dots [32] and concentration-dependent UV-vis absorption spectra of UA-CQDs, we adopted face-to-face configurations to construct the corresponding dimer structures to simulate the close packing in the solid state.

Based on the optimized structures **(Fig. 3a, Supplementary Figs. 15 and S16)**, both the monomer A-CQDs and its dimer 2-A-CQDs remain essentially planar. In contrast, in NTA-CQDs and BTA-CQDs, the triphenylamine unit, (naphthalene)-C(CN)=CH- unit, and (biphenyl)-C(CN)=CH- unit all form dihedral angles of 36.0°, 28.4°, and 33.3°, respectively. In the corresponding dimers, 2-NTA-CQDs and 2-BTA-CQDs, these dihedral angles range from 32.2° to 35.1°, 28.1°, and 41.6°. 2-A-CQDs, 2-NTA-CQDs, and 2-BTA-CQDs show an increasing trend in interlayer distances, with theoretical values of 3.38 Å, 3.52 Å, and 3.59 Å, respectively. Visually, the calculated PL spectra of three CQD models under

monomer and dimer conditions were plotted **(Figs. 3b and 3c)**. The plots show that the CQDs are endowed with excellent solid-state fluorescence properties by the passivation of the aromatic framework with triphenylamine, (naphthalene)-C(CN)=CH-, and (biphenyl)-C(CN)=CH- units. The fluorescence intensity of 2-BTA-CQDs is significantly enhanced by the structural differences between naphthalene and biphenyl, with almost no change in the emission peak position.

To further analyze the distinct electronic properties, analyses of hole-electron distribution and quantitative molecular orbital calculations were conducted **(Supplementary Fig. 17)**. The D-index represents the distance between the centroids of holes and electrons, and the overlap function S_r measures their spatial correlation. Compared to 2-A-CQDs (D = 0.000 Å, S_r = 0.876), a significantly enhanced spatial charge separation is observed in 2-NTA-CQDs (D = 4.772 Å, S_r = 0.145) and 2-BTA-CQDs (D = 4.164 Å, S_r = 0.212). A more complex excitation process is suggested, with mixed characteristics of localized excitons (LE) and charge transfer (CT). These results indicate that the unique structural units introduced in UA-CQDs enhance CT within and between CQDs upon excitation. This mechanism is key to their excellent solid-state fluorescence and is highly favorable for achieving superior electroluminescent (EL) performance.

The solid-state fluorescence enhancement strategy is shown in **Fig. 3d**. The introduction of triphenylamine, (naphthalene)-C(CN)=CH-, and (biphenyl)-C(CN)=CH- units **(Fig. 3e)** generates pronounced steric hindrance via induced dihedral angles. This hindrance effectively suppresses the direct π–π stacking of the aromatic cores. Consequently, larger interlayer spacing within the CQDs and increased interparticle distances are maintained, which collectively mitigate fluorescence quenching. Notably, compared to the naphthalene structure, the twisted biphenyl structure amplifies this steric effect through the non-planar extension of its molecular structure, leading to more efficient suppression of π–π interactions. These results reveal the solid-state fluorescence characteristics of UA-CQDs and elucidate the origin of the significantly enhanced optical performance of B-UA-CQDs.

Optical Properties of UA-CQDs

Further optical characterizations of the structurally engineered UA-CQDs were conducted. Given that the emission peak aligns with the absorption edges and exhibits excitation-independent characteristics in solution **(Supplementary Fig. 18)**, the emission can be attributed to intrinsic bandgap transitions within the conjugated π-domain. Furthermore, UA-CQDs exhibit a pronounced solvatochromic effect **(Supplementary Fig. 19)**, following the same trend as conventional organic luminescent materials: as the solvent polarity increases, the excited state with a larger dipole moment is stabilized, the bandgap narrows, and the emission peak progressively red-shifts. In solution, as the concentration increases, the UV-vis absorption spectra of UA-CQDs **(Supplementary Fig. 20)** exhibit a blue-shifted and broadened band-edge absorption peaks. This spectral change indicates a growing propensity for face-to-face stacking, ultimately giving rise to spectroscopic signatures characteristic of H-aggregates at higher concentrations [33]. Concomitantly, the PL spectra **(Supplementary Fig. 21)** show decreased in intensity and red-shifted emission peaks. These changes are attributed to the enhanced π–π stacking interactions and the resultant reduction in intermolecular distances as the CQDs aggregate.

Compared to their solution state, both UA-CQDs in the solid state **(Fig. 4a)** demonstrate a red shift in their emission peak, emitting bright yellow fluorescence with a peak at 570 nm and an FWHM of 62 nm for B-UA-CQDs, a peak at 569 nm and an FWHM of 66 nm for N-UA-CQDs. This red shift originates from the reduced spacing between CQDs, leading to interparticle stacking and coupling of edge structures, thereby narrowing the energy gap. Similar to their dissolved and film states, UA-CQDs exhibit excitation-independent characteristics in the solid state, as confirmed by the two-dimensional pseudocolor PL spectra

(Figs. 4b and 4c), which show nearly identical emission peaks across different excitation wavelengths. To quantify the difference in fluorescence intensity, solid-state PLQY tests were performed on the UA-CQD powders **(Fig. 4d)**. The results indicate that the PLQY of B-UA-CQDs is increased by 63% relative to N-UA-CQDs, fully demonstrating that the structural engineering for enhancing steric hindrance is effective. Whereas conventional CQDs show shortened lifetimes in the solid state due to significant non-radiative decay [34], as reveals by the time-resolved PL (TRPL) tests in **Fig. 4e and Supplementary Fig. 23b**, both UA-CQDs exhibit longer carrier lifetimes in the solid state compared to the film state. This demonstrates their ability to suppress non-radiative transitions and suggests potentially more efficient charge transfer processes.

Temperature-dependent PL spectra **(Figs. 4f and 4g)** of UA-CQDs powders (from 87 K to 333 K) reveal that the PL intensity of both UA-CQDs gradually increases at low temperatures, which is attributed to the suppression of non-radiative recombination effects triggered by exciton dissociation [35]. N-UA-CQDs exhibit secondary peaks emerging at approximately 600 nm and 660 nm at lower temperatures, likely originating from strong electron-phonon coupling effects [36]. In contrast, B-UA-CQDs maintain a single dominant emission peak, which undergoes a red shift to 590 nm below 173 K. This shift may result from a combination of the emergence of a secondary peak and the red shift of the primary peak. Furthermore, we estimated the exciton binding energy for both UA-CQDs using the Arrhenius equation:

$$I(T) = \frac{I_0}{1 + A\,exp\left(-\frac{E_b}{k_B T}\right)} \quad (1)$$

where $I(T)$ and I_0 are the integrated PL intensities at different temperatures and 0 K, A is a frequency factor, and k_B is the Boltzmann constant [37]. The fitting results **(Fig. 4h)** indicate that the exciton binding energies (E_b) of B-UA-CQDs and N-UA-CQDs are 153.5 meV and 84.7 meV, respectively. This demonstrates that excitons in B-UA-CQDs are more strongly confined, suppressing dissociation and thereby improving PL performance [38].

To investigate the luminescence mechanism and identify the reasons for the performance enhancement, we conducted femtosecond transient absorption (fs-TA) spectroscopy measurements using a probe wavelength ranging from 380 to 750 nm and a scan delay time ranging from 0.05 ps to 3.0 ns **(Supplementary Fig. 24)**. The spectra show two negative peaks in the 420–460 nm and 490–530 nm ranges, which are assigned to ground-state bleaching (GSB) and stimulated emission (SE), respectively. These peaks are consistent with the absorption and PL spectra measured in the same 1,4-dioxane solution. The positive peak in the 555–710 nm range corresponds to excited-state absorption (ESA). Global dynamics fittings were performed for both UA-CQDs **(Fig. 4i)**, revealing two decay components in each case. The short lifetimes (5.2 ps, 4.7 ps) are attributed to CQDs excited by pump light with photon energy exceeding the bandgap energy, where excess carrier energy drives Coulomb interactions toward thermal equilibrium. Subsequent optical and acoustic phonon scattering disperses carriers to the lowest excited state. The long lifetimes (162 ps, 128 ps) correspond to the process where cooled carriers emit fluorescence through radiative recombination. The complete TA processes of two types of CQDs are shown in **Figs. 4j and 4k** (without chirp correction). The decay kinetics of the peak centered at 510 nm **(Fig. 4l)** exhibit single-exponential decay, and B-UA-CQDs show a notably longer fluorescence lifetime than N-UA-CQDs.

Device structure and performance

The excellent solid-state fluorescence and favorable solubility of two types of UA-CQDs inspired the development of high-performance, low-cost CQD-LEDs. First, the spin-coated CQD films were

characterized by AFM and scanning electron microscopy (SEM) **(Supplementary Figs. 25 and 26)**. The films exhibit smooth surfaces with root mean square (RMS) values of 0.46 nm and 0.47 nm, respectively, facilitating the fabrication of high-performance devices. The band gaps of both UA-CQDs were calculated to be approximately 2.65 eV and 2.66 eV for B-UA-CQDs and N-UA-CQDs **(Supplementary Figs. 27a and 27b)**, using the equation $E_g^{opt} = 1240/\lambda_{edge}$. Additionally, the positive slope of the Mott-Schottky (M-S) plot **(Supplementary Fig. 28)** confirms the *n*-type semiconductor characteristics of both UA-CQDs.
The fabricated devices consist of an indium tin oxide (ITO) anode, PEDOT:PSS as the hole injection layer, an emitting layer employing either pristine UA-CQDs or a host-guest system with UA-CQDs as the guest, and PO-T2T as the electron transport layer, which possesses a high charge carrier mobility of 1.7×10^{-3} $cm^2\ V^{-1}\ s^{-1}$ and a deep HOMO level, facilitating charge carrier injection and transport. A bilayer structure of Cs_2CO_3/Al is used as the cathode **(Figs. 5a and 5b)**.
First, neat UA-CQDs were employed as the emissive layer to construct devices with a relatively simple architecture. The undoped devices exhibit stable electroluminescence with an emission peak at 538 nm and a FWHM of 96 nm, achieving a peak luminance of 7774 cd m^{-2}, an external quantum efficiency (EQE) of 0.33%, and a record-low V_{on} of 2.4 V **(Supplementary Fig. 29)**. To the best of our knowledge, this luminance represents the highest value and the V_{on} the lowest among undoped CQD-LEDs with an emission peak below 570 nm, confirming the superior optical properties of the structurally engineered B-UA-CQDs and highlighting their great potential. Additionally, space-charge-limited current (SCLC) measurements were performed using pristine UA-CQDs as the emissive layer **(Supplementary Fig. 30)**. By testing the corresponding hole-only and electron-only devices, the results indicate that B-UA-CQDs exhibit a higher electron mobility than N-UA-CQDs, which may help balance charge transport in devices where hole transport typically dominates.
Furthermore, it can be observed that devices using pristine CQDs as the emitting layer still suffer from low EQE despite achieving a relatively high maximum luminance, which is mainly attributed to conventional triplet exciton losses. Therefore, a thermally activated sensitized fluorescence (TSF) strategy was adopted. By utilizing TADF materials as the host, both singlet and triplet exciton energies captured by the host can be transferred to the guest CQDs via Förster resonance energy transfer (FRET), significantly improving exciton utilization. This strategy has been successfully applied in CQD-LEDs in recent years [17,39]. Based on the favorable performance of UA-CQDs and the TSF mechanism, highly efficient CQD-LEDs were developed. CzAcSF was selected as the host material, and 2 wt.% UA-CQDs were employed as the guest to construct a host-guest system, which exhibits good film-forming ability and efficient, relatively balanced energy levels for charge carrier transport. All fabricated CQD-LEDs all exhibit voltage-independent green electroluminescence. For B-UA-CQD-based devices, the EL emission peak is located at 505 nm, while that for N-UA-CQD-based devices is at 506 nm. The spectral shapes are nearly identical **(Fig. 5c and Supplementary Fig. 31)**. This emission differs from the cyan emission of CzAcSF **(Supplementary Fig. 32)**, and no shoulder peaks or parasitic emission are observed, demonstrating efficient energy transfer from the TADF host to UA-CQDs and excellent spectral stability. Notably, B-UA-CQD-based LEDs achieve a record-breaking EQE of 12.2% and a current efficiency of 37 cd A^{-2} **(Fig. 5d and Supplementary Fig. 33)**, surpassing all previously reported CQD-LEDs **(Supplementary Table 2)**. Moreover, even at a high luminance approaching 2000 cd m^{-2}, the device retains a high EQE of 9.2%, and its peak luminance reaches over 8300 cd m^{-2}. By comparison, N-UA-CQD-based LEDs achieve an EQE of 7.7% and a current efficiency of 24 cd A^{-1}. The superior device performance of B-UA-CQDs fully demonstrates the effectiveness of our structural engineering strategy: the extension and enlargement of steric hindrance significantly enhance solid-state PL, and this strategy

proves equally effective under EL conditions. Furthermore, device structure optimization was performed on the hole transport side. The hole injection layer was prepared using a poly(sodium 4-styrenesulfonate) (PSSNa)-modified PEDOT:PSS. PSSNa, the sodium salt of poly(styrene sulfonic acid), is a non-conductive component. By adding a controlled amount of PSSNa, the conductivity was regulated within a reasonable range to improve carrier balance [40,41]. Based on this adjustment, a peak luminance of 19,043 cd m^{-2} was achieved in our LEDs while maintaining stable monochromatic EL **(Fig. 5e and Supplementary Fig. 34)**. Meanwhile, a current efficiency of 19 cd A^{-1} and an EQE of 6.4% were obtained, still significantly outperforming conventional CQD-LEDs, which typically exhibit an EQE below 5%. Through structural engineering of CQDs and device optimization, record-breaking EQE values and peak luminance were achieved in B-UA-CQD-based devices **(Fig. 5f)**.

Motivated by the excellent performance of small-area rigid devices, we further explored the application prospects of UA-CQDs by fabricating large-area LEDs, flexible LEDs, and patterned LEDs **(Figs. 5g–5i)** [42,43]. Based on the excellent luminescent properties and film-forming ability of B-UA-CQDs, large-area devices (20×20 mm^2) exhibit uniform and bright green emission. For the flexible LEDs, bright green emission was maintained under various bending conditions. In addition, patterned LEDs with a pixel size of 15×15 μm^2 and a corresponding pixel density of approximately 1500 PPI were fabricated. The patterned LEDs maintain the uniform bright green emission of standard devices, with well-defined pixels and virtually no dead pixels. To the best of our knowledge, this is the first application of CQDs in patterned LEDs. These specialized LEDs demonstrate the remarkable potential of UA-CQDs for advanced display applications.

In summary, we have presented a simple ultrasound-assisted synthesis approach for the rapid production of bright solid-state fluorescent UA-CQDs under ambient conditions. By replacing a naphthalene-based precursor with a biphenyl-based counterpart, we significantly enhanced the solid-state PLQY by 63%. DFT calculations revealed that triphenylamine, naphthalene-acetonitrile, and biphenylacetonitrile form a sterically hindered three-dimensional architecture with possible CT characteristics, effectively suppressing π–π stacking-induced fluorescence quenching. The biphenyl moiety was identified as key to this anti-quenching effect. Taking advantage of the excellent optical properties and oil solubility of UA-CQDs enabled the fabrication of high-performance green LEDs. B-UA-CQD-based LEDs achieved an record-high EQE of 12.2%. Furthermore, through simple PEDOT:PSS modification, a high peak luminance of 19,043 cd m^{-2} was realized, representing the highest value ever reported for CQD-LEDs. This work offers a novel ultrasonic synthesis route for fabricating solid-state fluorescent CQDs and provides an effective strategy for improving CQD-LED performance at the emissive material level.

Methods

Synthesis of B-UA-CQDs and N-UA-CQDs

In a round-bottom flask (100 mL), 4,4'-diformyltriphenylamine (0.10 g, 0.33 mmol) and either 4-biphenylacetonitrile (0.10 g, 0.52 mmol, for B-UA-CQDs) or 2-naphthylacetonitrile (0.10 g, 0.60 mmol, for N-UA-CQDs) were dissolved completely in anhydrous ethanol (40 mL) under ultrasonication. Subsequently, sodium hydroxide (0.1 g, 2.50 mmol) was added. The reaction mixture was then subjected to ultrasonic irradiation (40 kHz, 240 W) for 0.5 h. Following the formation of a bright yellow fluorescent precipitate, the crude product was collected by centrifugation and washed three times with 75% ethanol. The product was further purified by silica gel column chromatography using dichloromethane as the eluent to yield the target CQDs. This synthetic procedure is readily scalable to gram quantities.

Device fabrication

First, ITO-coated glass substrates were ultrasonically cleaned in dish soap, water, acetone, and isopropanol, respectively. The substrates were dried with high-purity nitrogen and then moved to an ultraviolet ozone cleaning machine for 20 min to improve the ITO work function and surface energy. For the modified PEDOT:PSS hole injection layer, PSSNa was added to the PEDOT:PSS aqueous solution to prepare a 15 mg mL^{-1} solution. The resulting solution was filtered through a 0.45 μm filter, then spin-coated onto ITO substrates at 3000 rpm for 40 s, and annealed at 150 °C for 15 min. Unmodified PEDOT:PSS layers were prepared following the same spin-coating and annealing conditions, except that no PSSNa was added. The emitting layer was prepared by spin-coating a solution of UA-CQDs and CzAcSF (8 mg mL^{-1} in 1,4-dioxane) at different mixing ratios, at 2000 rpm for 30 s and annealed at 60 °C for 10 min. The substrate was transferred to a vacuum evaporation machine and evacuated to 5×10^{-4} Pa, and then PO-T2T, Cs_2CO_3, and Al were evaporated, respectively, and the film thicknesses were 50nm, 1 nm, and 100 nm, respectively.

Data availability

Source data are provided with this paper.

References

1 Kim, T. S. *et al.* Future trends of display technology: micro-LEDs toward transparent, free-form, and near-eye displays. *Light-Sci. Appl.* **14**, 355 (2025).

2 Zhou, H. *et al.* Exciplex-enabled high-efficiency, fully stretchable OLEDs. *Nature* **649**, 604-611 (2026).

3 Behrman, K. & Kymissis, I. Micro light-emitting diodes. *Nat. Electron.* **5**, 564-573 (2022).

4 Ma, D. *et al.* Distribution control enables efficient reduced-dimensional perovskite LEDs. *Nature* **599**, 594-598 (2021).

5 Dai, X. *et al.* Solution-processed, high-performance light-emitting diodes based on quantum dots. *Nature* **515**, 96-99 (2014).

6 Jang, E. & Jang, H. Review: Quantum Dot Light-Emitting Diodes. *Chem. Rev.* **123**, 4663-4692 (2023).

7 Xu, X. *et al.* Electrophoretic analysis and purification of fluorescent single-walled carbon nanotube fragments. *J. Am. Chem. Soc.* **126**, 12736-12737 (2004).

8 Liu, H. *et al.* A review of carbon dots in synthesis strategy. *Coord. Chem. Rev.* **498**, 215468 (2024).

9 Liu, Y. *et al.* Recent Advances in Highly Luminescent Carbon Dots. *Adv. Funct. Mater.* **35**, 2420587 (2024).

10 Geng, B. *et al.* Near-infrared phosphorescent carbon dots for sonodynamic precision tumor therapy. *Nat. Commun.* **13**, 5735 (2022).

11 Li, J. *et al.* Emancipating Target-Functionalized Carbon Dots from Autophagy Vesicles for a Novel Visualized Tumor Therapy. *Adv. Funct. Mater.* **28**, 1800881 (2018).

12 Hong, G., Diao, S., Antaris, A. L. & Dai, H. Carbon Nanomaterials for Biological Imaging and Nanomedicinal Therapy. *Chem. Rev.* **115**, 10816-10906 (2015).

13 Zhang, Y. *et al.* Solid-State Red Laser with a Single Longitudinal Mode from Carbon Dots. *Angew. Chem. Int. Ed.* **60**, 25514-25521 (2021).

14 Zhang, Y. *et al.* Carbon Dots with Blue-to-Near-Infrared Lasing for Colorful Speckle-Free Laser Imaging and Dynamical Holographic Display. *Adv. Mater.* **35**, 2302536 (2023).

15 Simões, R., Rodrigues, J., Neto, V., Monteiro, T. & Gonçalves, G. Carbon Dots: A Bright Future as

Anticounterfeiting Encoding Agents. *Small* **20**, 2311526 (2024).
16 Li, C., Li, J., Teng, Q., Li, J. & Yuan, F. Single Solid-State Emissive Carbon Quantum Dots for Multicolor, Bright and Efficient Electroluminescent Light-Emitting Diodes. *Angew. Chem. Int. Ed.* **64**, e202419983 (2024).
17 Li, C., Yang, Y. & Yuan, F. Unprecedented Matrix-Induced Emission Enhancement Enables Bright and Efficient Carbon Quantum Dot-Based Electroluminescent Light-Emitting Diodes. *Adv. Funct. Mater.* **36**, e24329 (2025).
18 Mason, T. J. Ultrasound in synthetic organic chemistry. *Chem. Soc. Rev.* **26**, 443-451 (1997).
19 Li, H. *et al.* One-step ultrasonic synthesis of water-soluble carbon nanoparticles with excellent photoluminescent properties. *Carbon* **49**, 605-609 (2011).
20 Wang, N. *et al.* Fluorine-doped carbon nitride quantum dots: Ethylene glycol-assisted synthesis, fluorescent properties, and their application for bacterial imaging. *Carbon* **109**, 141-148 (2016).
21 Xu, X. *et al.* Ultrasonication-Assisted Ambient-Air Synthesis of Monodispersed Blue-Emitting $CsPbBr_3$ Quantum Dots for White Light Emission. *ACS Appl. Nano Mater.* **2**, 6874-6879 (2019).
22 Dou, Y. *et al.* Ten-Gram-Scale Synthesis of $FAPbX_3$ Perovskite Nanocrystals by a High-Power Room-Temperature Ultrasonic-Assisted Strategy and Their Electroluminescence. *Adv. Mater. Technol.* **5**, 1901089 (2020).
23 Zhao, W., Wang, Y., Liu, K., Zhou, R. & Shan, C. Multicolor biomass based carbon nanodots for bacterial imaging. *Chin. Chem. Lett.* **33**, 798-802 (2022).
24 Ban, H. *et al.* ZnMgO Nanoparticles via Ultrasonic-Assisted Synthesis for Electron Transport Layer in InP-Based QD-LEDs. *ACS Appl. Nano Mater.* **7**, 11274-11284 (2024).
25 Ding, B. *et al.* Highly bright and ultra-stable cyan-emitting perovskite quantum dots encapsulated in zeolitic imidazolate framework-11 for advanced optoelectronic applications. *Chem. Eng. J.* **518**, 164706 (2025).
26 Chen, J., Zhao, H., Li, Z., Zhao, X. & Gong, X. Highly efficient tandem luminescent solar concentrators based on eco-friendly copper iodide based hybrid nanoparticles and carbon dots. *Energy Environ. Sci.* **15**, 799-805 (2022).
27 Miao, X. *et al.* Synthesis of Carbon Dots with Multiple Color Emission by Controlled Graphitization and Surface Functionalization. *Adv. Mater.* **30**, 1704740 (2017).
28 Kachwal, V. *et al.* Simple ratiometric push–pull with an 'aggregation induced enhanced emission' active pyrene derivative: a multifunctional and highly sensitive fluorescent sensor. *New J. Chem.* **42**, 1133-1140 (2018).
29 Zheng, Y. *et al.* Multicolor Carbon Dots Prepared by Single-Factor Control of Graphitization and Surface Oxidation for High-Quality White Light-Emitting Diodes. *Adv. Opt. Mater.* **9**, 2100688 (2021).
30 Zhang, Y. *et al.* Heteroatom-Doping and Conjugation-Extension Enable Ultrahigh-Bright Full-Color Carbon Quantum Dots for Tunable Liquid-State Lasers and 3D Printing. *Adv. Mater.* **38**, e03728 (2025).
31 Xu, K. *et al.* Solvent-free synthesis of oil-soluble fluorescent carbon dots for bright photoluminescent and electroluminescent light-emitting diodes. *Chem. Eng. J.* **470**, 144112 (2023).
32 Zhao, B. *et al.* Triphenylamine-Derived Solid-State Emissive Carbon Dots for Multicolor High-Efficiency Electroluminescent Light-Emitting Diodes. *Angew. Chem., Int. Ed.* **62**, e202301651 (2023).
33 Hestand, N. J. & Spano, F. C. Expanded Theory of H- and J-Molecular Aggregates: The Effects of

Vibronic Coupling and Intermolecular Charge Transfer. *Chem. Rev.* **118**, 7069-7163 (2018).
34 Zheng, M. *et al.* Gram-Scale Room-Temperature Synthesis of Solid-State Fluorescent Carbon Nanodots for Bright Electroluminescent Light Emitting Diodes. *Small* **19**, 2206715 (2023).
35 Zhu, H. *et al.* Enriched-Bromine Surface State for Stable Sky-Blue Spectrum Perovskite QLEDs With an EQE of 14.6%. *Adv. Mater.* **34**, 2205092 (2022).
36 Wang, B. *et al.* Electron–phonon coupling-assisted universal red luminescence of o-phenylenediamine-based carbon dots. *Light-Sci. Appl.* **11**, 172 (2022).
37 Feng, Y. *et al.* Nucleophilic Reaction-Enabled Chloride Modification on $CsPbI_3$ Quantum Dots for Pure Red Light-Emitting Diodes with Efficiency Exceeding 26 %. *Angew. Chem. Int. Ed.* **63**, e202318777 (2024).
38 Li, C., Yang, Y., Li, J. & Yuan, F. Nitrogen/Oxygen Co-Doped Carbon Quantum Dots with Efficient High Color-Purity Red Emission for Bright Electroluminescent LEDs. *Angew. Chem. Int. Ed.* **64**, e202513847 (2025).
39 Teng, Q., Tan, Q., Hou, M. & Yuan, F. Thermally Activated Sensitized Fluorescence Enables Efficient Carbon Quantum Dot-Based Electroluminescent LEDs with Current Efficiency of 31 cd A−1. *Angew. Chem. Int. Ed.* **64**, e202508650 (2025).
40 Liu, W. Z. *et al.* Enhancing Carrier Balance in Blade-Coated Near-Infrared Quantum Dot Light-Emitting Diodes by a PSS-Rich PEDOT:PSS Hole-Buffering Layer. *Small* **21**, e04662 (2025).
41 Chu, Z. *et al.* Blue light-emitting diodes based on quasi-two-dimensional perovskite with efficient charge injection and optimized phase distribution via an alkali metal salt. *Nat. Electron.* **6**, 360-369 (2023).
42 Chen, Z. *et al.* Rigid crosslinker-assisted nondestructive direct photolithograph for patterned QLED displays. *Light-Sci. Appl.* **14**, 251 (2025).
43 Sha, S. *et al.* Aqueous/Alcohol-Soluble Carbon Dot Light-Emitting Diodes. *Adv. Mater.* **38**, e73773 (2026).

Acknowledgements
The authors appreciate the support of the Excellent Going Abroad Experts' Training Program in Hebei Province. The authors thank Xin Zhang and Kaiyao Liu (Hebei University) for their support in the fabrication and characterization of LED devices, and Jiahua Hu (Zhengzhou University) for providing the software tools that enabled fs-TA spectroscopic data processing.

Funding
J.Z. discloses support for the research of this work from the Advanced Talents Incubation Program of Hebei University [grant number 050001-521100225205]. X.L. discloses support for the research of this work from the National Natural Science Foundation of China [grant number 62575094].

Author Contributions
Z.L. and J.Z. wrote the manuscript. Z.L. drew the figures. J.L. and L.G. performed theoretical calculations. Z.L., B.L., and L.Z. synthesized CQDs and fabricated/characterized CQD-LEDs. Z.T. advised the manuscript. X.L. and J.Z. advised the manuscript and supervised the investigations. All authors participated in the discussion and commented on the manuscript.

Competing Interests Statements

The authors declare no competing interests.

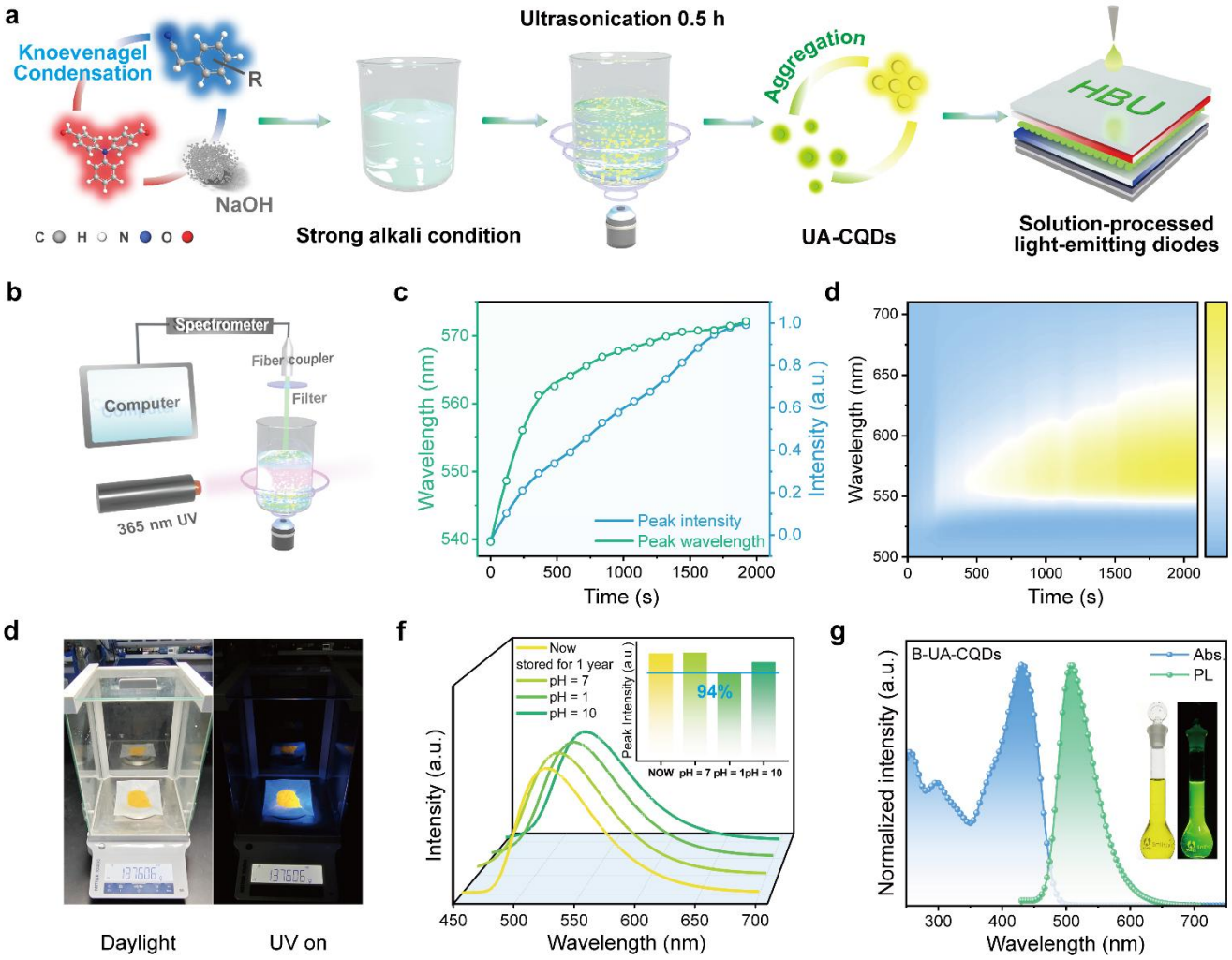


Fig. 1 Synthesis and characterization of UA-CQDs. (a) Synthesis and application of UA-CQDs. **(b)** Schematic diagram of *in situ* PL monitoring. **(c)** Reaction-time-dependent changes of the peak wavelength and intensity. **(d)** *In situ* PL spectra. **(e)** Optical photo of gram-scale UA-CQDs powder under daylight (left) and UV light (right). **(f)** PL spectra of UA-CQDs stored for one year in different solutions. **(g)** Normalized absorption and PL spectra of B-UA-CQDs, and images of the solution under daylight (left) and UV light (right).

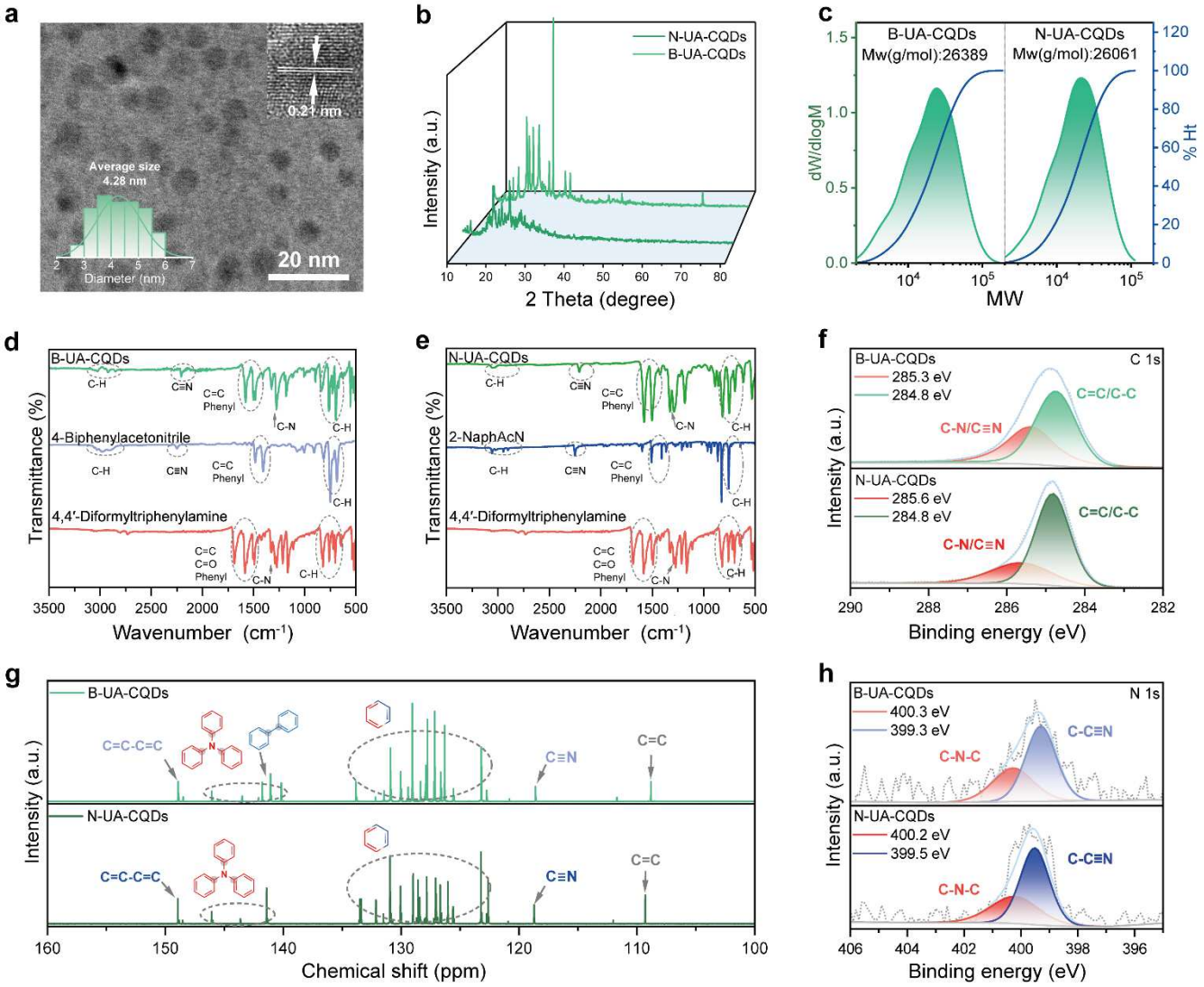


Fig. 2 Structural characterization of UA-CQDs. (a) TEM image of B-UA-CQDs. Inserts present the corresponding HRTEM image and diameter histogram. **(b)** XRD patterns of UA-CQDs. **(c)** Molecular weight distributions of UA-CQDs. FT-IR spectra of (**d**) B-UA-CQDs and **(e)** N-UA-CQDs along with their corresponding precursors. **(f)** High-resolution C 1s spectra of UA-CQDs. **(h)** High-resolution N 1s spectra of UA-CQDs. **(g)** ^{13}C NMR signals of UA-CQDs.

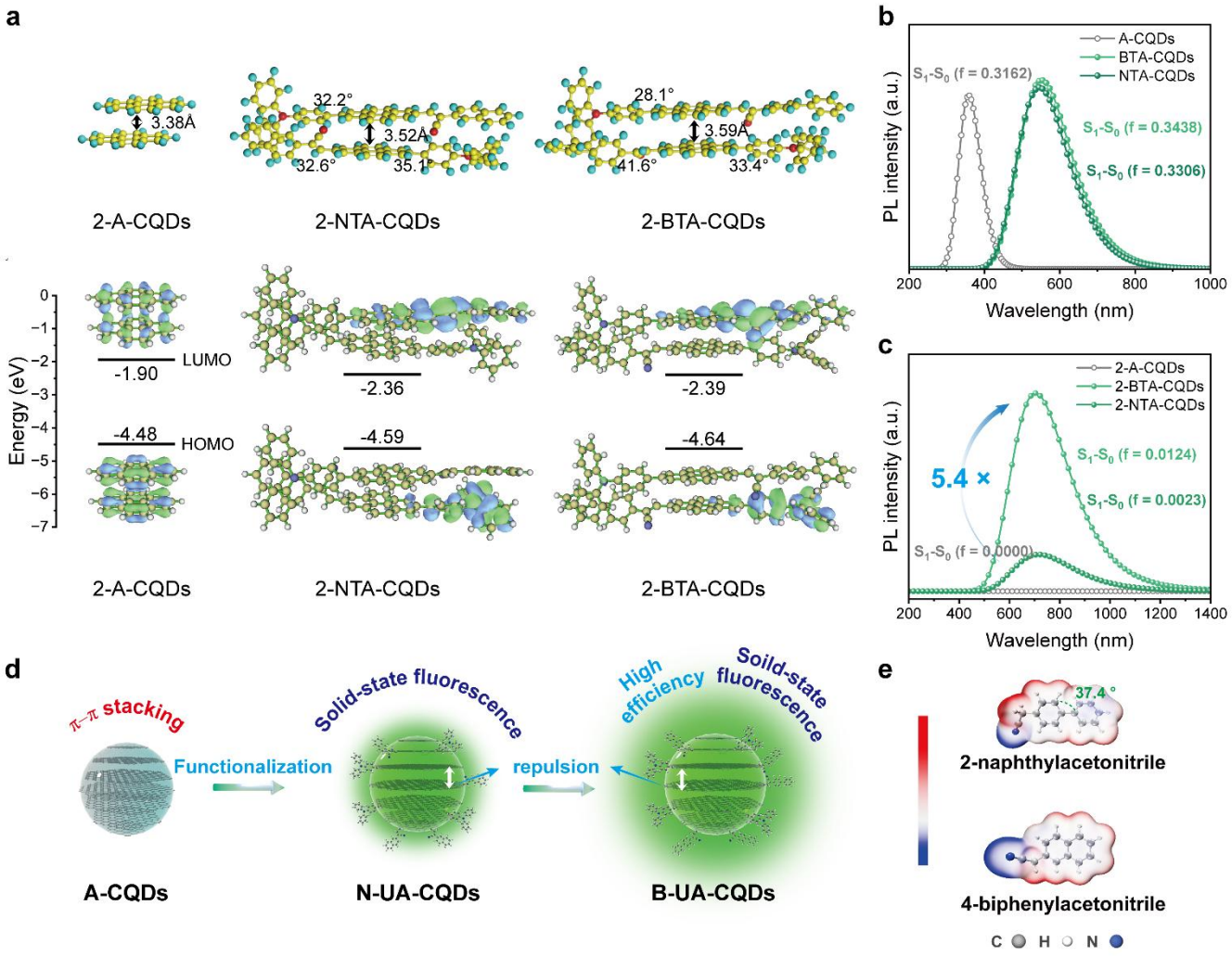


Fig. 3 DFT calculations. (a) Calculated optimized structure and HOMO/LUMO distribution of 2-A-CQDs, 2-NTA-CQDs, and 2-BTA-CQDs. PL spectra (the Gaussian broadening of the first excited state (S_1-S_0)) of **(b)** A-CQDs, NTA-CQDs, and BTA-CQDs, and **(c)** 2-A-CQDs, 2-NTA-CQDs, and 2-BTA-CQDs. **(d)** Schematic diagram of structural engineering strategy for UA-CQDs. **(e)** Electrostatic potential map of the precursors.

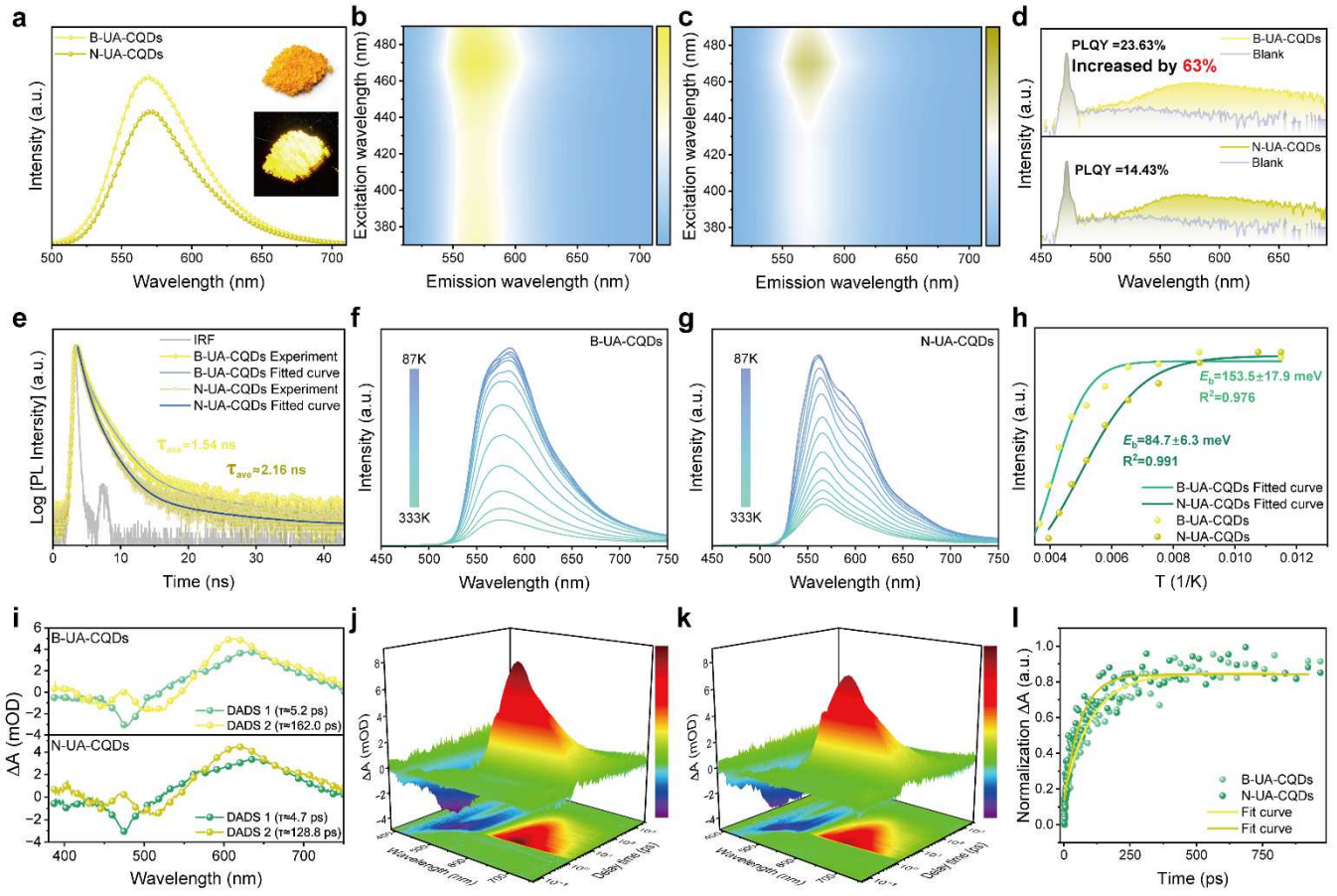


Fig. 4 Optical characteristics of UA-CQDs. (a) PL spectra in the solid state of UA-CQDs and images of the B-UA-CQDs under daylight (up) and UV light (down). Two-dimensional pseudocolor map of normalized excitation-dependent PL spectra of **(b)** B-UA-CQDs and **(c)** N-UA-CQDs. **(d)** The PLQY of UA-CQDs in the solid state under 470 nm excitation. **(e)** Time-resolved PL spectra of UA-CQDs in the solid state. Temperature-dependent PL spectra from 87 K to 333 K of **(f)** B-UA-CQDs and **(g)** N-UA-CQDs. **(h)** The exciton binding energy fitted by the Arrhenius equation. **(i)** TA spectra with global fitting results with two exponent decay functions. Three-dimensional colour-mapped surface plot illustrating the TA spectra of **(j)** B-UA-CQDs and **(k)** N-UA-CQDs. **(l)** Kinetic fitting curve at 510 nm.

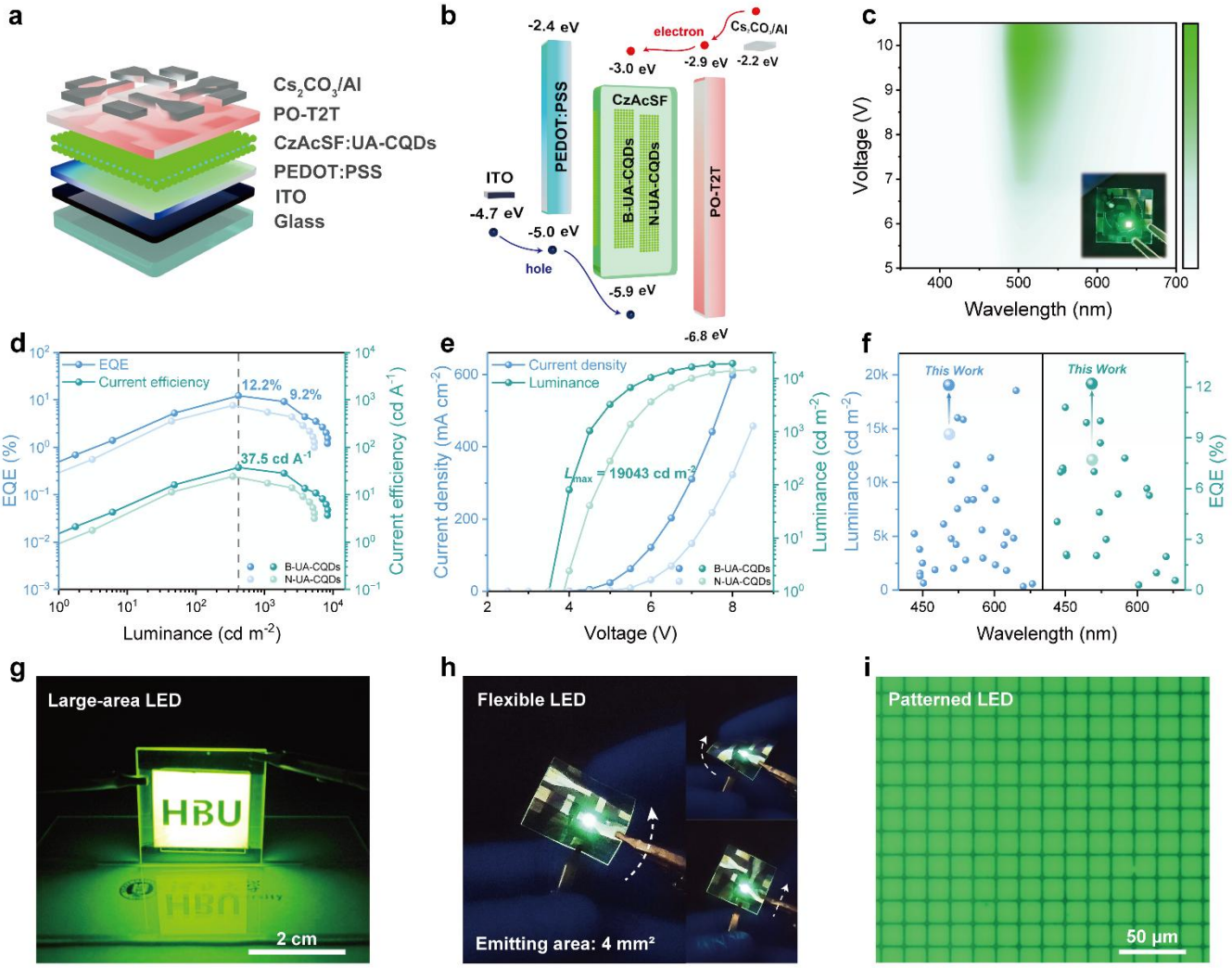


Fig. 5 Structure and performance of UA-CQD-based LEDs. (a) Device structure. **(b)** Energy level diagram. **(c)** Two-dimensional pseudocolor map of EL spectra and the photograph of the device during operation for B-UA-CQD-based LEDs. For LEDs based on B-UA-CQDs and N-UA-CQDs: **(d)** EQE and current efficiency as functions of luminance; **(e)** *J*-*V*-*L* characteristics of devices using m-PEDOT:PSS as the hole transport layer. **(f)** Performance comparison of the fabricated device with other reported CQD-LEDs. B-UA-CQD-based LEDs: **(g)** Large-area LED, **(h)** Flexible LED, and **(i)** Patterned LED.

Supplementary Files

This is a list of supplementary files associated with this preprint. Click to download.

- SupplementaryInformation.docx